How to cite: *Angew. Chem. Int. Ed.* **2020**, *59*, 20589 – 20595
International Edition: doi.org/10.1002/anie.202008787
German Edition: doi.org/10.1002/ange.202008787

VIP **Single-Atom Catalysis** **Very Important Paper**

Single-Atom Electrocatalysts from Multivariate Metal–Organic Frameworks for Highly Selective Reduction of CO_2 at Low Pressures

*Long Jiao, Weijie Yang, Gang Wan, Rui Zhang, Xusheng Zheng, Hua Zhou, Shu-Hong Yu, and Hai-Long Jiang**

Abstract: *Single-atom catalysts (SACs) are of great interest because of their ultrahigh activity and selectivity. However, it is difficult to construct model SACs according to a general synthetic method, and therefore, discerning differences in activity of diverse single-atom catalysts is not straightforward. Herein, a general strategy for synthesis of single-atom metals implanted in N-doped carbon (M_1-N-C; M = Fe, Co, Ni and Cu) has been developed starting from multivariate metal–organic frameworks (MOFs). The M_1-N-C catalysts, featuring identical chemical environments and supports, provided an ideal platform for differentiating the activity of single-atom metal species. When employed in electrocatalytic CO_2 reduction, Ni_1-N-C exhibited a very high CO Faradaic efficiency (FE) up to 96.8 % that far surpassed Fe_1-, Co_1- and Cu_1-N-C. Remarkably, the best-performer, Ni_1-N-C, even demonstrated excellent CO FE at low CO_2 pressures, thereby representing a promising opportunity for the direct use of dilute CO_2 feedstock.*

Introduction

Single-atom catalysts (SACs), as a new frontier of heterogeneous catalysis, have witnessed their great superiority in diverse reactions.[1–9] With the active sites dispersed at atomic level, SACs possess ultrahigh catalytic activity and selectivity and facilitate the understanding of the structure-performance relationship at atomic/molecular scale.[1–9] Generally, the catalytic performance of SACs is highly dependent on intrinsic properties of metal active sites and their surrounding microenvironment as well as physicochemical characteristics of supports, the latter of which pose great challenges to the nature identification of catalytic sites.[10–12] Specifically, single-atom metal decorated N-doped carbon (M_1-N-C) materials, an important subclass of SACs, have been recognized as excellent electrocatalysts for CO_2 reduction reaction (CO_2RR).[13–20] However, the carbon supports of the reported M_1-N-C materials always display various characteristics (pore structure, surface area, morphology, etc.), making the activity of M_1-N-C tends to vary considerably even with the same metal center.[21,22] On account of this, the general synthesis of M_1-N-C with a wide variety of metal species but similar microenvironment and supports is highly desired to identify the intrinsic activity of single-atom active sites.

Multivariate metal-organic frameworks (MTV-MOFs), an important subclass of MOFs incorporating multiple linkers of different functionalities within a single crystal, creating complexity within a skeleton in a controlled manner, have attracted growing attentions in many applications.[23–26] The diversity of constituent units in MTV-MOFs create huge opportunities for the general construction of M_1-N-C with various metal centers. Meanwhile, it is ready for MTV-MOFs to control the variables of their derivatives, such as morphology, pore structure, surface area, elemental content, etc. Therefore, MTV-MOFs are ideal candidates to construct SACs and exclusively identify the intrinsic activities of different metal centers for CO_2RR. Meanwhile, the porous feature of MOFs can be largely inherited to their derivatives, which will benefit the exposure of active sites and thereby CO_2RR performance.[27–29]

In addition to the active site identification, another critical issue in CO_2RR is the energy-consuming capture and purification process of CO_2. Specifically speaking, to achieve high selectivity, the currently reported CO_2RR are generally performed in pure CO_2.[30–42] However, the actual concentration of CO_2 feedstock available from industrial processes such as coal power plant (5–15 % CO_2) and steel/petrochemical industry (14–33 % CO_2) is relatively low.[43–45] Given the thermodynamic stability of the C=O bond (≈ 806 kJ mol^{-1}) of CO_2 and its limited solubility in aqueous solution, low CO_2 concentration will significantly affect the activity, setting great barriers for the direct CO_2 utilization.[45–47] Therefore, the development of efficient electrocatalysts for direct

[*] Dr. L. Jiao, R. Zhang, Prof. Dr. S.-H. Yu, Prof. Dr. H.-L. Jiang
Hefei National Laboratory for Physical Sciences at the Microscale
CAS Key Laboratory of Soft Matter Chemistry, Department of Chemistry, University of Science and Technology of China
Hefei, Anhui 230026 (P. R. China)
E-mail: jianglab@ustc.edu.cn
Dr. W. Yang
Department of Power Engineering, School of Energy, Power and Mechanical Engineering, North China Electric Power University
Baoding 071003 (P. R. China)
Dr. G. Wan
Materials Science Division, Argonne National Laboratory
Lemont, IL 60439 (USA)
Dr. X. Zheng
National Synchrotron Radiation Laboratory
University of Science and Technology of China
Hefei, Anhui 230029 (P. R. China)
Dr. H. Zhou
X-ray Science Division, Advanced Photon Source
Argonne National Laboratory
Lemont, IL 60439 (USA)
Supporting information and the ORCID identification number(s) for the author(s) of this article can be found under: https://doi.org/10.1002/anie.202008787.

conversion of CO_2 at low pressures is extremely significant. However, such technology remains in its infancy and therefore this is rarely achieved.[43,45]

With all of the aforementioned points in mind, a series of isostructural porphyrinic MTV-MOFs constructed from M-TCPP (M = Fe, Co, Ni and Cu; TCPP = tetrakis (4-carboxyphenyl)porphyrin) and H_2-TCPP were selected as precursors. Thanks to the isomorphism of MTV-MOFs and spatial isolation of metal centers in M-TCPP, four kinds of M_1-N-C (M = Fe, Co, Ni and Cu) materials, featuring single metal atoms with a very similar carbon support environment, have been obtained upon pyrolysis and serve as model catalysts to compare the intrinsic activity of diverse single-atom metal species (Scheme 1). Among all four M_1-N-C (M = Fe, Co, Ni and Cu) model catalysts for electrocatalytic CO_2RR, Ni_1-N-C exhibits the highest CO Faradic efficiency (FE) of 96.8% with a turnover frequency (TOF) up to 11315 h^{-1} at −0.8 V in pure CO_2. Theoretical calculations reveal that Ni_1-N-C possesses the most positive value of the limiting potential difference between CO_2 reduction and H_2 evolution among all four M_1-N-C catalysts, elucidating its high CO_2RR selectivity in experiments. Remarkably, the best-performer—the Ni_1-N-C catalyst—is able to catalyze the reduction of diluted CO_2, though a very challenging task, and it presented and excellent CO FE even at 30% and 15% CO_2 concentrations. These results strongly prove the great superiority of Ni_1-N-C toward selective CO_2 reduction under practical conditions.

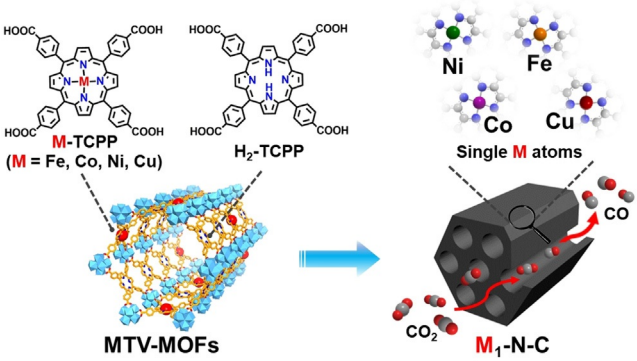

Scheme 1. Illustration showing the general fabrication of single-atom M_1-N-C catalysts based on MTV-MOFs for electrocatalytic CO_2 reduction.

Results and Discussion

Synthesis and characterization of M_1-N-C

A family of isostructural porphyrinic MTV-MOFs, named M-PCN-222 (M = Fe, Co, Ni and Cu), have been successfully constructed by M-TCPP (M = Fe, Co, Ni and Cu) and H_2-TCPP via the mixed ligand strategy (Supporting Information, Figure S1).[28] With the general synthetic approach, the obtained M-PCN-222 involving different M-TCPP ligands present uniform rod-like shape with similar particle sizes, surface area and pore structure (Figure 1a; Figures S2 and S3). Upon the pyrolysis of M-PCN-222 followed by ZrO_2 removal, M_1-N-C (M = Fe, Co, Ni and Cu) can be finally obtained. Taking Ni_1-N-C as a representative, it shows a rod-like shape with a diameter of ≈200 nm, similar to those of Fe_1-, Co_1- and Cu_1-N-C (Figure 1b; Figure S4). In addition, no obvious metal nanoparticle is found in the TEM images of M_1-N-C (Figure 1b; Figure S4). N_2 adsorption measurements indicate that all M_1-N-C possess similar surface area and pore size distribution (Supporting Information, Figure S5, Table S2). Powder X-ray diffraction (XRD) patterns of all M_1-N-C present two broad peaks corresponding to the (002) and (101) planes of carbon and no peaks of metallic phase can be observed, in accordance with TEM results (Figure S6). In the Raman spectra of all M_1-N-C catalysts, the intensity ratios of D band (1345 cm^{-1}) and G band (1590 cm^{-1}) are subject to small oscillation from 0.92 to 0.94, illustrating their similar graphitization degree (Figure S7, Table S2).

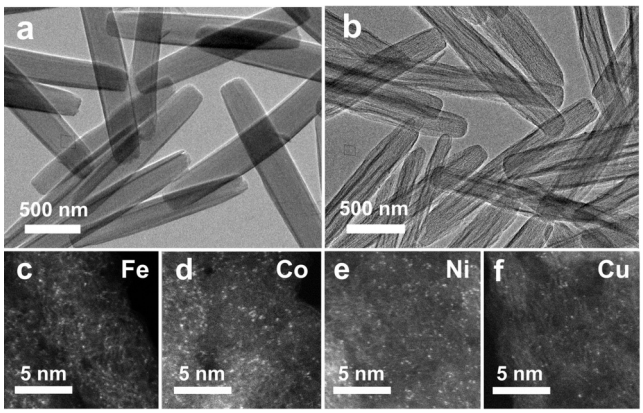

Figure 1. Transmission electron microscopy (TEM) images of a) Ni-PCN-222 and b) Ni_1-N-C. The aberration-corrected HAADF-STEM images of c) Fe_1-N-C, d) Co_1-N-C, e) Ni_1-N-C and f) Cu_1-N-C.

X-ray photoelectron spectroscopy (XPS) was adopted to investigate the chemical compositions and electronic states of M_1-N-C catalysts. The fitted N 1 s XPS spectrum of Ni_1-N-C clearly shows five characteristic peaks including pyridinic N (398.7 eV), Ni-N moieties (399.4 eV), pyrrolic N (400.2 eV), graphitic N (401.1 eV) and oxidized N (402.6 eV) species (Figure S8a), confirming the existence of Ni–N bonding.[28,48] The Ni $2p_{3/2}$ of Ni_1-N-C presents a binding energy (855.4 eV) located between Ni^0 (853.0 eV) and Ni^{2+} (855.7 eV), illustrating the partially oxidized Ni species originated from Ni-N species (Figure S9a).[19,49] Moreover, the N K-edge near-edge X-ray absorption fine structure (NEXAFS) analysis has been further conducted. For the metal-free N-doped carbon (N-C) derived from PCN-222 involving H_2-TCPP linker only, two π* peaks corresponding to pyridinic N (peak a) and graphitic N (peak b), as well as a broaden peak (peak c) related to C-N σ* bond, are detected (Figure S10a).[50,51] In contrast, peak a broadens and splits into double peaks (a_1 and a_2) in Ni_1-N-C, suggesting the existence of Ni atoms stabilized by pyridinic N (Figure 2a).[51] Supportive results of XPS and N K-edge NEXAFS spectra are also obtained for Fe_1-, Co_1- and Cu_1-N-C catalysts, all demonstrating the formation of corresponding M-N species (Figures S8, S9 and S10a). Quantitatively, the N content and Ni loading in Ni_1-N-C are

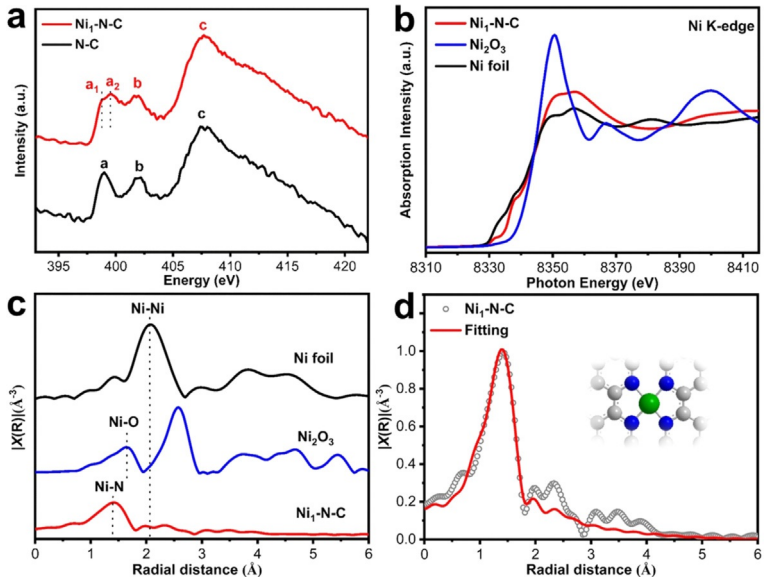

Figure 2. Structural characterizations. a) N K-edge NEXAFS spectrum, b) Ni K-edge XANES spectrum, c) k^2-weighted FT-EXAFS spectrum and d) EXAFS fitting of the Ni_1-N-C and optimized coordination environment of Ni atoms (inset).

determined to be 4.94 and 1.75 wt%, similar to the other M_1-N-C (M = Fe, Co and Cu) catalysts (Table S2). In the aberration-corrected high-angle annular dark field scanning transmission electron microscope (HAADF-STEM) images, all M_1-N-C catalysts are featured with bright dots randomly dispersed in the selected area, clearly presenting the full of atomically dispersed metal species in the domain of each M_1-N-C (Figures 1c–f).

Atomic structure analysis by X-ray absorption spectroscopy (XAS)

To gain more information on the chemical environments of single metal atoms in M_1-N-C, X-ray absorption spectroscopy (XAS) was carried out. Taking Ni_1-N-C as an example, the adsorption edge of Ni_1-N-C in the Ni-K edge XANES spectra locates between Ni foil and Ni_2O_3, manifesting the positive charge state of Ni in Ni_1-N-C, in consistence with the XPS result (Figure 2b; Figure S9a). In the Fourier transform-extended X-ray absorption fine structure (FT-EXAFS) spectrum of Ni_1-N-C, only one dominated peak at 1.4 Å associated to the Ni-N scattering path is presented and no Ni-Ni bond ($\approx$2.07 Å) can be observed, verifying the formation of singe-atom Ni sites in Ni_1-N-C (Figure 2c). The EXAFS fitting suggests that the Ni is coordinated by four N atoms (Figure 2d; Table S3). The XAS analyses have been performed on Fe_1-, Co_1- and Cu_1-N-C as well and the results illustrate that all M_1-N-C possess similar metal coordination environment, featuring single-atom M coordinated by four N atoms (Figures S10 and S11, Table S3).

Electrocatalytic performance for CO_2RR in pure CO_2

Encouraged by the above results, the M_1-N-C materials indeed feature almost identical structures except for different single metal atom sites. Therefore, they are ideal model catalysts to decode the intrinsic properties of these single-atom metals, by deducting their similar microenvironment and support factors, in electrochemical CO_2 reduction. As revealed by the linear sweep voltammetry (LSV) curves, Ni_1-N-C offers a much larger current response in pure CO_2 stream than the other M_1-N-C catalysts, indicating the significantly higher activity of Ni_1-N-C toward CO_2RR (Figure 3a; Figures S12–S14). Furthermore, the Faradaic efficiencies (FEs) for M_1-N-C catalysts at different potentials have been investigated. The Ni_1-N-C shows the best CO selectivity with a highest CO FE of 96.8% at −0.8 V among all M_1-N-C catalysts (Figure 3b). Meanwhile, the high CO FE (over 90%) of Ni_1-N-C can be maintained in a wide potential range from −0.65 V to −0.95 V with H_2 as the only byproduct (no detectable liquid product), manifesting the excellent selectivity of Ni_1-N-C for CO_2RR (Figure 3b; Figures S15 and S16). The Fe_1-N-C catalyst is the second most active catalyst with a highest CO FE of 86.5%. In comparison, the remaining two catalysts, Co_1-N-C and Cu_1-N-C, display much lower CO FE caused by the very competitive HER process (Figure 3b; Figure S15). Moreover, the TOF and CO partial current density (J_{CO}) of Ni_1-N-C reach 11315 h^{-1} and 27 mA cm^{-2} at −0.8 V, far surpassing those of the other three M_1-N-C catalysts (Figure 3c; Figure S17). In fact, Ni_1-N-C shows a smaller Tafel slope (98 mV/decade) than that of Fe_1-(104 mV/decade), Co_1- (142 mV/decade) and Cu_1-N-C (118 mV/decade), indicating the more favorable kinetics of Ni_1-N-C (Figure 3d). Meanwhile, Ni_1-N-C also shows smaller charge transfer resistance and larger electrochemical active surface area (ECSA) than other M_1-N-C catalysts, further supporting its much higher catalytic activity (Figures S18 and S19). In addition, the best performed Ni_1-N-C exhibits a long-term stability at −0.8 V for 10 h without obvious decay in current density and FE of CO (Figure 3e). The distinctly different performance of M_1-N-C model catalysts not only

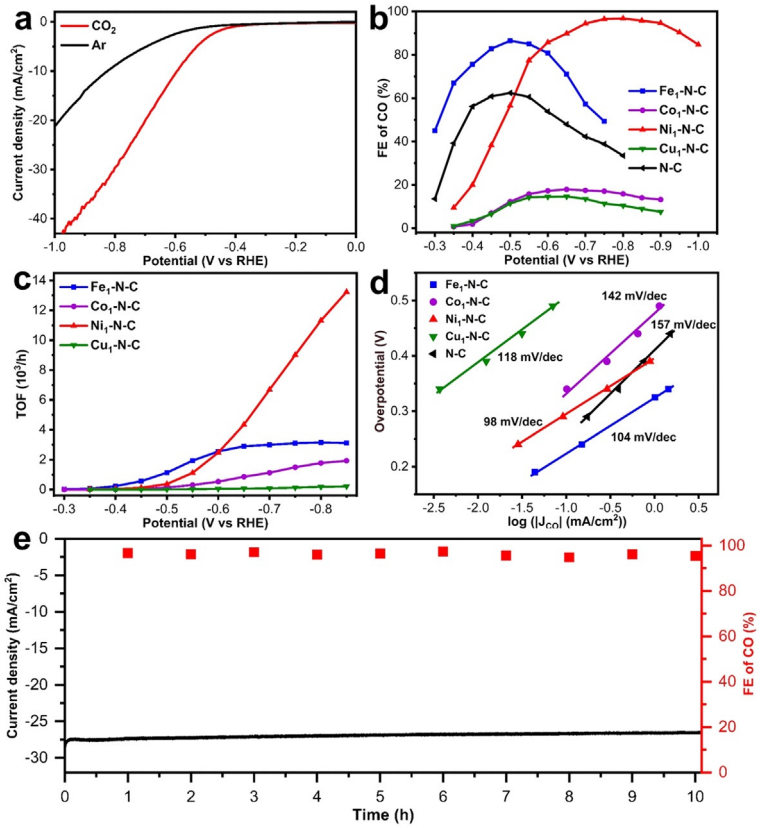

Figure 3. Electrochemical performances in pure CO_2. a) LSV curves of Ni_1-N-C in pure Ar- and CO_2-saturated 0.5 M $KHCO_3$. b) FEs and c) TOFs of M_1-N-C for CO in pure CO_2-saturated 0.5 M $KHCO_3$. d) Tafel plots of M_1-N-C for CO_2RR. e) Durability test of Ni_1-N-C at a constant potential of −0.8 V vs. RHE in pure CO_2.

reveals that the catalytic activity and selectivity are strongly dependent on active metal species, but also unambiguously demonstrates that single-atom Ni site far exceeds the other metal sites in M_1-N-C. This conclusion is of significant yet being achieved previously, given the complexity of different SACs with different structural parameters such as metal loading, surface area, pore structure, coordination environment, etc. For better comparison, the metal-free N-C prepared from the PCN-222, with similar structural characteristics as M_1-N-C, has also been synthesized (Figures S1–S7, Tables S1 and S2). It can be seen that N-C shows much lower current response, CO FE and turnover number (TON) and larger Tafel slope than Ni_1-N-C for CO_2 reduction, further supporting the importance role of single Ni atoms (Figures 3b,d; Figures S20 and S21). Furthermore, Ni_1-N-C also shows better current response and CO FE than mix-Ni-N-C, the latter of which is derived from the mixture of Ni-TCPP and H_2-TCPP, further demonstrating the superiority of MOFs as precursors (Figure S22).

Theoretical study of M_1-N-C in CO_2RR

The above control experiments clearly demonstrate that all structural parameters in M_1-N-C catalysts are almost identical except for different metals. Therefore, M_1-N-C virtually provide ideal models for density functional theory (DFT) calculations to achieve reliable mechanism of diverse single-atom metal centers toward CO_2RR. Generally, the generation of CO by CO_2RR takes place in the following steps: (i) the CO_2 adsorption; (ii) the formation of *COOH; (iii) the formation of *CO and (iv) the CO desorption (* represents adsorbed intermediates; Figure 4a).[40,52,53] Among the four elementary reaction steps, the formation of *COOH is calculated to be the rate-determining step (RDS) for all M_1-N-C catalysts (Figure 4b; Figures S23 and S24). In all investigated M_1-N-C catalysts, Ni_1-N-C and Fe_1-N-C present much lower energy barriers for *COOH formation than Co_1-N-C and Cu_1-N-C, manifesting the much higher activity of Ni_1-N-C and Fe_1-N-C for CO_2 reduction (Figure 4b; Figure S25). In addition, Ni_1-N-C also shows much lower energy barrier for CO desorption than Fe_1-N-C, illustrating the faster CO release from Ni_1-N-C (Figure 4b; Figure S25). All above support the highest activity of Ni_1-N-C for CO_2 reduction. Given the existence of competitive HER process, the limiting potential difference between CO_2RR and HER ($U_L(CO_2)$-$U_L(H_2)$; $U_L = -\Delta G_0/e$) has been further calculated and employed as the descriptor of CO selectivity, where more positive value of $U_L(CO_2)$-$U_L(H_2)$ represents a higher CO_2RR selectivity than hydrogen evolution.[35,54,55] As shown in Figure 4c, the $U_L(CO_2)$-$U_L(H_2)$ values for Fe_1-, Co_1-, Ni_1- and Cu_1-N-C are −1.15, −1.98, −1.19 and −2.33 eV,

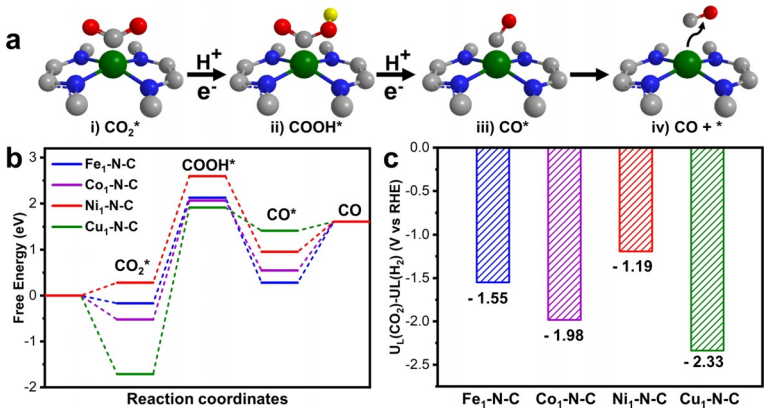

Figure 4. DFT calculations. a) Reaction paths and b) free energy diagrams of CO_2 reduction to CO. c) The values of $U_L(CO_2)$-$U_L(H_2)$ for all M_1-N-C catalysts.

respectively, which explains the CO selectivity following the order of Ni_1-N-C > Fe_1-N-C > Co_1-N-C > Cu_1-N-C, in high consistence with the experimental results (Figure 3b).

Electrocatalytic performance in CO_2RR at low pressures

On the basis of the experimental evidences and theoretical calculations above, Ni_1-N-C incorporated with Ni-N_4 sites is highly efficient in selective CO_2 reduction. Inspired by this, the electrocatalytic performance of Ni_1-N-C toward low-concentration CO_2 reduction, which is a very challenging target in CO_2RR, has been further investigated. Prior to electrocatalytic measurements, the concentrations of protons ($[H^+]$) and dissolved CO_2 ($[CO_2(aq)]$) in aqueous solution under different CO_2 concentrations are calculated in detail based on dissociation equilibrium theories and Henry's law (Figure S26). Obviously, the $[H^+]$ and $[CO_2(aq)]$ concentrations decrease significantly under lower CO_2 pressures, making CO_2 reduction more difficult according to the reaction equilibrium ($CO_2(aq) + 2H^+ + 2e^- \rightleftharpoons CO + H_2O$). Moreover, the equilibrium potentials are calculated based on the Nernst equation to be negatively shifted by 46 and 73 mV when CO_2 partial pressure decreased from 1 atm to 0.3 and 0.15 atm (Figure S27). The calculations conclude that the CO_2RR will be much more difficult at low CO_2 partial pressures from the viewpoint of thermodynamics. Therefore, this raises a higher demand for both activity and selectivity of the electrocatalysts, toward addressing this challenging goal.

In the experimental results, the LSV curves of Ni_1-N-C in CO_2/Ar mixed gas containing 30% and 15% CO_2 reasonably present higher current responses than that in pure Ar, indicating the evident CO_2 reduction activity under diluted CO_2 (Figure 5a). Using 30% CO_2 as the feed gas, the maximal CO FE of Ni_1-N-C reaches 91.6% with J_{CO} and TOF values of 6.69 mA cm^{-2} and 1395 h^{-1} at −0.8 V (Figure 5b and S28). Even though the concentration of CO_2 lowers to 15%, a high CO FE (83.2%) can still be observed at −0.75 V with J_{CO} and TOF of 2.91 mA cm^{-2} and 607 h^{-1} (Figure 5b; Figure S28). It can be seen that even though the CO partial current density goes down with decreased CO_2 concentration, the CO FE still reaches above 80% under 15% CO_2 (Figure 5b; Figure S29). In addition to the main product of CO, a small amount of H_2 as the only byproduct (no liquid product) can be detected at low CO_2 concentrations (Figures S30 and S16), similar to that in pure CO_2. Furthermore, Ni_1-N-C possesses stable current densities and CO FEs over 10 h at 30% and 15% CO_2 concentrations (Figure 5c). The results above clearly demonstrate the great potential of Ni_1-N-C for highly selective CO_2 reduction by using dilute CO_2 feedstock from industrial processes.

Conclusion

In summary, a series of single-atom catalysts (M_1-N-C, M = Fe, Co, Ni and Cu), exhibiting almost identical pore structures and compositions, were constructed from isostructural porphyrinic MTV-MOFs. The obtained M_1-N-Cs, featuring a very similar microenvironment and support effect for metal active sites, were employed as ideal model catalysts to identify the intrinsic properties of single-atom metal species in electrochemical CO_2 reduction. Under pure CO_2 conditions, Ni_1-N-C, with single-atom Ni as the active center, manifests the most satisfactory CO_2RR performances with the highest CO selectivity up to 96.8%, followed by Fe_1-N-C, Co_1-N-C and Cu_1-N-C. DFT calculations support the activity trend and illustrate that the best performing catalyst, Ni_1-N-C, with the most positive value of $U_L(CO_2)$-$U_L(H_2)$, can efficiently promote CO_2RR and suppress the competitive HER. Given the ultrahigh selectivity of SACs, Ni_1-N-C has also been employed to catalyze the reduction of CO_2 at low pressures, which is more challenging and rarely reported. Strikingly, Ni_1-N-C maintains high selectivity even at 30% and 15% CO_2, which are practical concentrations that are directly available from industrial processes, further suggesting the superiority and ultrahigh selectivity of Ni_1-N-C for CO_2RR. This work provides a general route to a broad class of model SACs, which can eliminate the interference of microenvironment and support effects, thereby unambiguously unveiling the superior intrinsic performance of single Ni atoms compared to Fe, Co and Cu in M_1-N-C for CO_2RR.

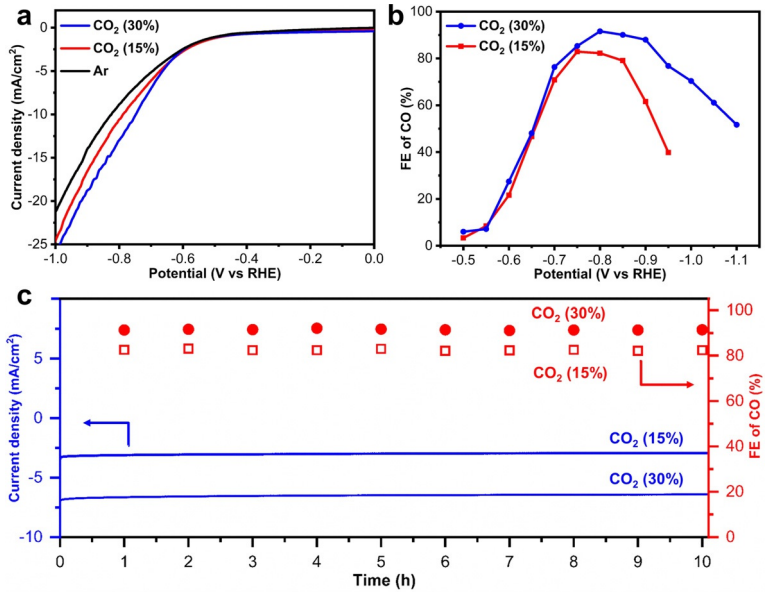

Figure 5. Electrochemical performances of CO_2 at low pressures. a) LSV curves and b) CO FE of Ni_1-N-C in 0.5 M $KHCO_3$ saturated with 30% and 15% CO_2. c) Durability tests of Ni_1-N-C at a constant potential of −0.8 V under 30% CO_2 concentration and −0.75 V under 15% CO_2 concentration, respectively.

Moreover, the preliminary results herein highlight the great potential of Ni-based SACs for direct electrocatalytic CO_2 conversion at low concentrations.

Acknowledgements

This work was supported by the NSFC (21725101, 21871244 and 21521001), China Postdoctoral Science Foundation (2019TQ0298, 2019M660151), International Partnership Program of CAS (211134KYSB20190109) and Fundamental Research Funds for the Central Universities (WK2060030029). Use of the Advanced Photon Source was supported by the U.S. Department of Energy, Office of Science, Office of Basic Energy Sciences, under Contract No. DE-AC02-06CH11357, and the Canadian Light Source and its funding partners. The calculations in this work were supported by the Supercomputing Center of the University of Science and Technology of China.

Conflict of interest

The authors declare no conflict of interest.

Keywords: CO_2 reduction · electrocatalysis · low pressure · metal–organic frameworks

[1] A. Wang, J. Li, T. Zhang, *Nat. Rev. Chem.* **2018**, *2*, 65 – 81.
[2] J. Liu, *ACS Catal.* **2017**, *7*, 34 – 59.
[3] S. Ji, Y. Chen, X. Wang, Z. Zhang, D. Wang, Y. Li, *Chem. Rev.* **2020**, https://doi.org/10.1021/acs.chemrev.9b00818.
[4] C. Zhu, Q. Shi, S. Feng, D. Du, Y. Lin, *ACS Energy Lett.* **2018**, *3*, 1713 – 1721.
[5] X. Li, X. Yang, Y. Huang, T. Zhang, B. Liu, *Adv. Mater.* **2019**, *31*, 1902031.
[6] H. Zhang, G. Liu, L. Shi, J. Ye, *Adv. Energy Mater.* **2018**, *8*, 1701343.
[7] L. Zhang, Y. Jia, G. Gao, X. Yan, N. Chen, J. Chen, M. T. Soo, B. Wood, D. Yang, A. Du, X. Yao, *Chem* **2018**, *4*, 285 – 297.
[8] L. Jiao, H.-L. Jiang, *Chem* **2019**, *5*, 786 – 804.
[9] C. Tang, Y. Jiao, B. Shi, J.-N. Liu, Z. Xie, X. Chen, Q. Zhang, S.-Z. Qiao, *Angew. Chem. Int. Ed.* **2020**, *59*, 9171 – 9176; *Angew. Chem.* **2020**, *132*, 9256 – 9261.
[10] L. Zhao, Y. Zhang, L.-B. Huang, X.-Z. Liu, Q.-H. Zhang, C. He, Z.-Y. Wu, L.-J. Zhang, J. Wu, W. Yang, L. Gu, J.-S. Hu, L.-J. Wan, *Nat. Commun.* **2019**, *10*, 1278.
[11] Y. Sun, L. Silvioli, N. R. Sahraie, W. Ju, J. Li, A. Zitolo, S. Li, A. Bagger, L. Arnarson, X. Wang, T. Moeller, D. Bernsmeier, J. Rossmeisl, F. Jaouen, P. Strasser, *J. Am. Chem. Soc.* **2019**, *141*, 12372 – 12381.
[12] X. He, Q. He, Y. Deng, M. Peng, H. Chen, Y. Zhang, S. Yao, M. Zhang, D. Xiao, D. Ma, B. Ge, H. Ji, *Nat. Commun.* **2019**, *10*, 3663.
[13] Y. Hou, Y.-B. Huang, Y.-L. Liang, G.-L. Chai, J.-D. Yi, T. Zhang, K.-T. Zang, J. Luo, R. Xu, H. Lin, S.-Y. Zhang, H.-M. Wang, R. Cao, *CCS Chem.* **2019**, *1*, 384 – 395.
[14] Y. Cheng, S. Zhao, B. Johannessen, J. P. Veder, M. Saunders, M. R. Rowles, M. Cheng, C. Liu, M. F. Chisholm, R. D. Marco, H. M. Cheng, S. Z. Yang, S. P. Jiang, *Adv. Mater.* **2018**, *30*, 1706287.
[15] T. Zheng, K. Jiang, N. Ta, Y. Hu, J. Zeng, J. Liu, H. Wang, *Joule* **2019**, *3*, 265 – 278.
[16] X. Rong, H.-J. Wang, X.-L. Lu, R. Si, T.-B. Lu, *Angew. Chem. Int. Ed.* **2020**, *59*, 1961 – 1965; *Angew. Chem.* **2020**, *132*, 1977 – 1981.
[17] J. Gu, C.-S. Hsu, L. Bai, H. M. Chen, X. Hu, *Science* **2019**, *364*, 1091 – 1094.
[18] T. Wang, Q. Zhao, Y. Fu, C. Lei, B. Yang, Z. Li, L. Lei, G. Wu, Y. Hou, *Small Methods* **2019**, *3*, 1900210.
[19] C. Yan, H. Li, Y. Ye, H. Wu, F. Cai, R. Si, J. Xiao, S. Miao, S. Xie, F. Yang, Y. Li, G. Wang, X. Bao, *Energy Environ. Sci.* **2018**, *11*, 1204 – 1210.
[20] X.-L. Lu, X. Rong, C. Zhang, T.-B. Lu, *J. Mater. Chem. A* **2020**, *8*, 10695 – 10708.

[21] H. Peng, F. Liu, X. Liu, S. Liao, C. You, X. Tian, H. Nan, F. Luo, H. Song, Z. Fu, P. Huang, *ACS Catal.* **2014**, *4*, 3797 – 3805.
[22] J. Li, P. Pršlja, T. Shinagawa, A. J. M. Fernández, F. Krumeich, K. Artyushkova, P. Atanassov, A. Zitolo, Y. Zhou, R. García-Muelas, N. López, J. Pérez-Ramírez, F. Jaouen, *ACS Catal.* **2019**, *9*, 10426 – 10439.
[23] H. Deng, C. J. Doonan, H. Furukawa, R. B. Ferreira, J. Towne, C. B. Knobler, B. Wang, O. M. Yaghi, *Science* **2010**, *327*, 846 – 850.
[24] A. Kirchon, L. Feng, H. F. Drake, E. A. Josepha, H.-C. Zhou, *Chem. Soc. Rev.* **2018**, *47*, 8611 – 8638.
[25] X. Kong, H. Deng, F. Yan, J. Kim, J. A. Swisher, B. Smit, O. M. Yaghi, J. A. Reimer, *Science* **2013**, *341*, 882 – 885.
[26] B. Li, H.-M. Wen, H. Wang, H. Wu, T. Yildirim, W. Zhou, B. Chen, *Energy Environ. Sci.* **2015**, *8*, 2504 – 2511.
[27] S. Dang, Q.-L. Zhu, Q. Xu, *Nat. Rev. Mater.* **2017**, *3*, 17075.
[28] L. Jiao, G. Wan, R. Zhang, H. Zhou, S.-H. Yu, H.-L. Jiang, *Angew. Chem. Int. Ed.* **2018**, *57*, 8525 – 8529; *Angew. Chem.* **2018**, *130*, 8661 – 8665.
[29] K. J. Lee, J. H. Lee, S. Jeoung, H. R. Moon, *Acc. Chem. Res.* **2017**, *50*, 2684 – 2692.
[30] J. Han, P. An, S. Liu, X. Zhang, D. Wang, Y. Yuan, J. Guo, X. Qiu, K. Hou, L. Shi, Y. Zhang, S. Zhao, C. Long, Z. Tang, *Angew. Chem. Int. Ed.* **2019**, *58*, 12711 – 12716; *Angew. Chem.* **2019**, *131*, 12841 – 12846.
[31] H. Yang, Q. Lin, C. Zhang, X. Yu, Z. Cheng, G. Li, Q. Hu, X. Ren, Q. Zhang, J. Liu, C. He, *Nat. Commun.* **2020**, *11*, 593.
[32] W. Luc, B. H. Ko, S. Kattel, S. Li, D. Su, J. G. Chen, F. Jiao, *J. Am. Chem. Soc.* **2019**, *141*, 9902 – 9909.
[33] A. Guan, Z. Chen, Y. Quan, C. Peng, Z. Wang, T.-K. Sham, C. Yang, Y. Ji, L. Qian, X. Xu, G. Zheng, *ACS Energy Lett.* **2020**, *5*, 1044 – 1053.
[34] J. Wu, Y. Huang, W. Ye, Y. Li, *Adv. Sci.* **2017**, *4*, 1700194.
[35] W. Ren, X. Tan, W. Yang, C. Jia, S. Xu, K. Wang, S. C. Smith, C. Zhao, *Angew. Chem. Int. Ed.* **2019**, *58*, 6972 – 6976; *Angew. Chem.* **2019**, *131*, 7046 – 7050.
[36] J. Li, Y. Kuang, Y. Meng, X. Tian, W.-H. Hung, X. Zhang, A. Li, M. Xu, W. Zhou, C.-S. Ku, C.-Y. Chiang, G. Zhu, J. Guo, X. Sun, H. Dai, *J. Am. Chem. Soc.* **2020**, *142*, 7276 – 7282.
[37] X. Wei, Z. Yin, K. Lyu, Z. Li, J. Gong, G. Wang, L. Xiao, J. Lu, L. Zhuang, *ACS Catal.* **2020**, *10*, 4103 – 4111.
[38] H. Zhong, M. Ghorbani-Asl, K. H. Ly, J. Zhang, J. Ge, M. Wang, Z. Liao, D. Makarov, E. Zschech, E. Brunner, I. M. Weidinger, J. Zhang, A. V. Krasheninnikov, S. Kaskel, R. Dong, X. Feng, *Nat. Commun.* **2020**, *11*, 1409.
[39] M. A. Ghausi, J. Xie, Q. Li, X. Wang, R. Yang, M. Wu, Y. Wang, L. Dai, *Angew. Chem. Int. Ed.* **2018**, *57*, 13135 – 13139; *Angew. Chem.* **2018**, *130*, 13319 – 13323.
[40] Q. Huang, Q. Li, J. Liu, Y.-R. Wang, R. Wang, L.-Z. Dong, Y.-H. Xia, J.-L. Wang, Y.-Q. Lan, *Matter* **2019**, *1*, 1656 – 1668.
[41] A. Vasileff, X. Zhi, C. Xu, L. Ge, Y. Jiao, Y. Zheng, S.-Z. Qiao, *ACS Catal.* **2019**, *9*, 9411 – 9417.
[42] A. Vasileff, Y. Zhu, X. Zhi, Y. Zhao, L. Ge, H. M. Chen, Y. Zheng, S.-Z. Qiao, *Angew. Chem. Int. Ed.* **2020**, https://doi.org/10.1002/anie.202004846; *Angew. Chem.* **2020**, https://doi.org/10.1002/ange.202004846.
[43] X. Wang, A. Xu, F. Li, S.-F. Hung, D.-H. Nam, C. M. Gabardo, Z. Wang, Y. Xu, A. Ozden, A. S. Rasouli, A. H. Ip, D. Sinton, E. H. Sargent, *J. Am. Chem. Soc.* **2020**, *142*, 3525 – 3531.
[44] G. V. Last, M. T. Schmick, *Environ. Earth Sci.* **2015**, *74*, 1189 – 1198.
[45] P. Hou, W. Song, X. Wang, Z. Hu, P. Kang, *Small* **2020**, *16*, 2001896.
[46] T. Nakajima, Y. Tamaki, K. Ueno, E. Kato, T. Nishikawa, K. Ohkubo, Y. Yamazaki, T. Morimoto, O. Ishitani, *J. Am. Chem. Soc.* **2016**, *138*, 13818 – 13821.
[47] Y. Wang, N.-Y. Huang, J.-Q. Shen, P.-Q. Liao, X.-M. Chen, J.-P. Zhang, *J. Am. Chem. Soc.* **2018**, *140*, 38 – 41.
[48] Y.-N. Gong, L. Jiao, Y. Qian, C.-Y. Pan, L. Zheng, X. Cai, B. Liu, S.-H. Yu, H.-L. Jiang, *Angew. Chem. Int. Ed.* **2020**, *59*, 2705 – 2709; *Angew. Chem.* **2020**, *132*, 2727 – 2731.
[49] C. Zhao, X. Dai, T. Yao, W. Chen, X. Wang, J. Wang, J. Yang, S. Wei, Y. Wu, Y. Li, *J. Am. Chem. Soc.* **2017**, *139*, 8078 – 8081.
[50] L. Jiao, Y. Hu, H. Ju, C. Wang, M.-R. Gao, Q. Yang, J. Zhu, S.-H. Yu, H.-L. Jiang, *J. Mater. Chem. A* **2017**, *5*, 23170 – 23178.
[51] P. Chen, T. Zhou, L. Xing, K. Xu, Y. Tong, H. Xie, L. Zhang, W. Yan, W. Chu, C. Wu, Y. Xie, *Angew. Chem. Int. Ed.* **2017**, *56*, 610 – 614; *Angew. Chem.* **2017**, *129*, 625 – 629.
[52] Z. Zhang, J. Xiao, X.-J. Chen, S. Yu, L. Yu, R. Si, Y. Wang, S. Wang, X. Meng, Y. Wang, Z.-Q. Tian, D. Deng, *Angew. Chem. Int. Ed.* **2018**, *57*, 16339 – 16342; *Angew. Chem.* **2018**, *130*, 16577 – 16580.
[53] P. Chen, Y. Jiao, Y.-H. Zhu, S.-M. Chen, L. Song, M. Jaroniec, Y. Zheng, S.-Z. Qiao, *J. Mater. Chem. A* **2019**, *7*, 7675 – 7682.
[54] D. Kim, C. Xie, N. Becknell, Y. Yu, M. Karamad, K. Chan, E. J. Crumlin, J. K. Nørskov, P. Yang, *J. Am. Chem. Soc.* **2017**, *139*, 8329 – 8336.
[55] C. Chen, X. Sun, X. Yan, Y. Wu, H. Liu, Q. Zhu, B. B. A. Bediako, B. Han, *Angew. Chem. Int. Ed.* **2020**, *59*, 11123 – 11129; *Angew. Chem.* **2020**, *132*, 11216 – 11222.

Manuscript received: June 23, 2020
Revised manuscript received: July 24, 2020
Accepted manuscript online: July 28, 2020
Version of record online: September 1, 2020

